ELSEVIER

Journal of Structural Geology 28 (2006) 2169–2181

JOURNAL OF STRUCTURAL GEOLOGY

www.elsevier.com/locate/jsg

Variability in Early Amazonian Tharsis stress state based on wrinkle ridges and strike-slip faulting

Chris H. Okubo [a,b,*], Richard A. Schultz [a]

[a] *Geomechanics—Rock Fracture Group, Department of Geological Sciences/174, University of Nevada, Reno, NV 89557-0138, USA*
[b] *Lunar and Planetary Laboratory, The University of Arizona, Tucson, AZ 85721-0063, USA*

Received 8 October 2004; received in revised form 7 September 2005; accepted 30 November 2005
Available online 25 January 2006

Abstract

We present evidence for a decrease in the magnitude of Tharsis-circumferential compressive stress during the Late Hesperian to the Middle Amazonian based on chronologic changes in the predominant style of faulting in southern Amazonis Planitia. Using high-resolution MOLA topography, we identify a population of strike-slip faults that exhibit Middle Amazonian-aged displacements of regional chrono-stratigraphic units. These strike-slip faults are adjacent to an older population of previously documented Late Hesperian-aged thrust faults (wrinkle ridges). Along-strike orientations of these thrust and strike-slip faults reveal the Tharsis-radial stress to be the area's most compressive remote principal stress and that this stress orientation and magnitude persisted throughout the Late Hesperian to the Middle Amazonian. We show that the change in the predominant style of faulting from thrust faulting to strike-slip faulting during this time requires a decrease of the Tharsis-circumferential compressive stress to a magnitude less than lithostatic load, with negligible change in stress orientation.

Keywords: Mars tectonics; Coulomb stress change; Thrust fault; Strike-slip; Wrinkle ridge

1. Introduction

Wrinkle ridges are widespread on Mars, and with a few localized exceptions, wrinkle ridge growth is generally constrained to within the Late Hesperian (Mangold et al., 2000; Tanaka et al., 2003). Given that normal faulting and graben formation appears to have occurred throughout much of Mars' history (Anderson et al., 2001), how and why was wrinkle ridge growth generally restricted to this limited period of time? In an effort to understand how wrinkle ridge growth began and ended, we evaluate temporal variations in the causative near-surface stress states from chronologically-distinct sets of cross-cutting wrinkle ridges and strike-slip faults along the periphery of the Tharsis rise in southern Amazonis Planitia.

Specific causative stress states correspond to particular styles of faulting (i.e. thrust, normal, or strike-slip faulting; Anderson, 1951). In this paper, inferred styles of faulting in southern Amazonis Planitia are used to predict causative stress states, providing a quantification of the orientations and relative magnitudes of the effective principal stresses that acted to drive the observed deformation. Two distinct styles of faulting are inferred in the study area: thrust faulting and strike-slip faulting. Thrust faults are commonly expressed at the ground surface through attendant fault-related fold topography. On planetary surfaces, such fault-related folds are commonly referred to as 'wrinkle ridges' (Schultz, 2000; Montési and Zuber, 2003; Okubo and Schultz, 2003, 2004; Mueller and Golombek, 2004), or as a morphometric sub-classification termed 'lobate scarps' (Watters and Robinson, 1999; Watters et al., 2000; Schultz and Watters, 2001). The interpretation of wrinkle ridges as the surface expressions of thrust fault-related

* Corresponding author. Present address: Lunar and Planetary Laboratory, The University of Arizona, Tucson, AZ 85721-0063, USA. Tel.:+1 520 626 1458; fax: +1 520 626 8998.
E-mail addresses: chriso@lpl.arizona.edu (C.H. Okubo), schultz@mines.unr.edu (R.A. Schultz).

0191-8141/$ - see front matter © 2005 Elsevier Ltd. All rights reserved.
doi:10.1016/j.jsg.2005.11.008

folds is supported by quantitative analyses of wrinkle ridge topography (Schultz, 2000; Okubo and Schultz, 2004), along with kinematic analyses of ridge and impact crater intersections (Sharpton and Head, 1988; Allemand and Thomas, 1992; Mangold et al., 1998). Strike-slip faulting on Mars has been previously identified based on photographic interpretations of strike-slip fault-related topography (Schultz, 1989; Artita and Schultz, 2005), as well as interpreted offsets of stratigraphy (Forsythe and Zimbelman, 1988) and wrinkle ridges (Schultz, 1989; Anguita et al., 2001).

In the following sections, we identify of a population of strike-slip faults through analyses of Mars Orbiter Laser Altimeter (MOLA)-based topography (cf. Smith et al., 2001) and provide independent lines of reasoning that justify these interpretations of strike-slip faulting. Causative stress states are then inferred. Based on the relative ages of the wrinkle ridges and strike-slip faults, temporal variations in the broader Tharsis-scale stresses are subsequently deduced. Finally, the implications of these results for models of Tharsis loading are discussed.

2. Observations

The study area is located in southern Amazonis Planitia, west of Olympus Mons (Fig. 1). This area is northwest of the Tharsis rise, but not on the topographic high. A potential strike-slip fault identified in Gordii Dorsum by Forsythe and Zimbelman (1988) is located ca. 500 km to the southeast. The area is within the northern lowlands, straddling the contact between Hesperian- and Amazonian-aged plains units (Fig. 2) (Tanaka et al., 2003).

Careful analysis of MOLA-based topography at 128 pixel/degree (ca. 435 m/pixel) resolution conducted by Tanaka et al. (2003) reveals a population of linear échelon scarps in the study area (Fig. 2a). These scarps can be grouped into two distinct sets by orientation, one set trending ca. N50°W and one trending ca. N60°E. Tanaka et al. (2003) interpret the N50°W scarp set as wrinkle ridges concentric about Olympus Mons. Further, Tanaka et al. (2003) observe that the scarps within the N60°E set show a distinct asymmetric sense of throw. The northern halves of these scarps show a down-to-the-east sense of throw, while the southern halves show a down-to-the-west sense of throw. Tanaka et al. (2003) interpret these scarps as the surface expressions of strike-slip faults, with an unspecified sense of displacement. This interpretation is based on (1) the linear surface expression of these scarps, (2) the oblique trend of these scarps to the interpreted wrinkle ridges of the N50°W set, (3) the termination of one of these N60°E scarps against a wrinkle ridge of the N50°W set, and (4) the orientation of these scarps within inferred causative stresses for the wrinkle ridges.

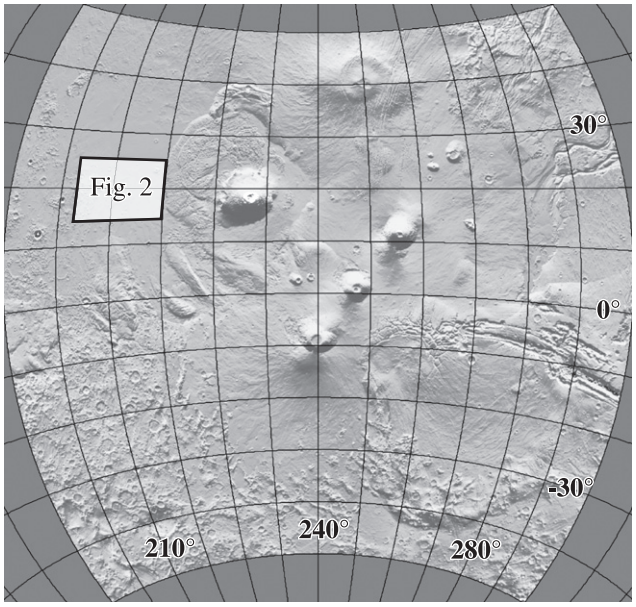

Fig. 1. MOLA-based shaded relief map of the western equatorial region of Mars showing the location of the study area (Fig. 2) relative to the large volcanoes of the Tharsis rise and Valles Marineris. Illumination is from the north, and the image is in an azimuthal equidistant projection.

Relative ages of both the N50°W- and N60°E-trending scarp sets are proposed by Tanaka et al. (2003) based on cross-cutting relations with local exposures of regional stratigraphic units. Based on regional mapping, Tanaka et al. (2003) propose stratigraphic units correlated with relative and surmised absolute ages based on crater density. Referring to their stratigraphic divisions, Tanaka et al. (2003) report that the N50°W scarp set ('wrinkle ridges') cross-cuts an older member of the smooth lobate unit 1 (Als_1), as well as the older lobate material (AHl) and boundary plains unit 2 (Hb_2). These scarps are, in turn, interpreted to be buried by younger lava flows of the smooth lobate unit 1 (Als_1). These relations indicated to Tanaka et al. (2003) that the N50°W 'wrinkle ridge' fault set was active during the Middle Amazonian. Further, the accompanying N60°E strike-slip fault set cross-cuts older lava flows of Als_1, as well as AHl, Hb_2, the younger unit of Als_1 and the N50°W 'wrinkle ridge' fault set. These relations implied to Tanaka et al. (2003) that strike-slip faulting occurred some time after activity along the 'wrinkle ridge' fault set. Such a change in the style of faulting could provide information into changes in the local stress state during the Middle Amazonian, which yield insight into changes in the local Tharsis-related stresses at that time.

In this study, a new MOLA-based DEM of the area (Fig. 2) is created in order to further investigate the initial findings of Tanaka et al. (2003). This DEM is based on the current (February 2003 release) version L processing level of the MOLA Precision Experiment Data Records (PEDRs; Smith et al., 2003). The MOLA data are gridded and interpolated to a continuous surface DEM at 200 pixel/degree resolution (ca. 279 m/pixel) using the methodology outlined by Okubo et al. (2004). In order to evaluate the broader regional context of the study area, this new DEM encompasses approximately 90% more geographic area than the DEM used by Tanaka et al. (2003).

Inspection of the DEM shown in Fig. 2 reveals that the scarps of the N50°W set, interpreted as wrinkle ridges by Tanaka et al. (2003), show asymmetric distributions of throw in similar fashion to Tanaka et al.'s interpreted strike-slip

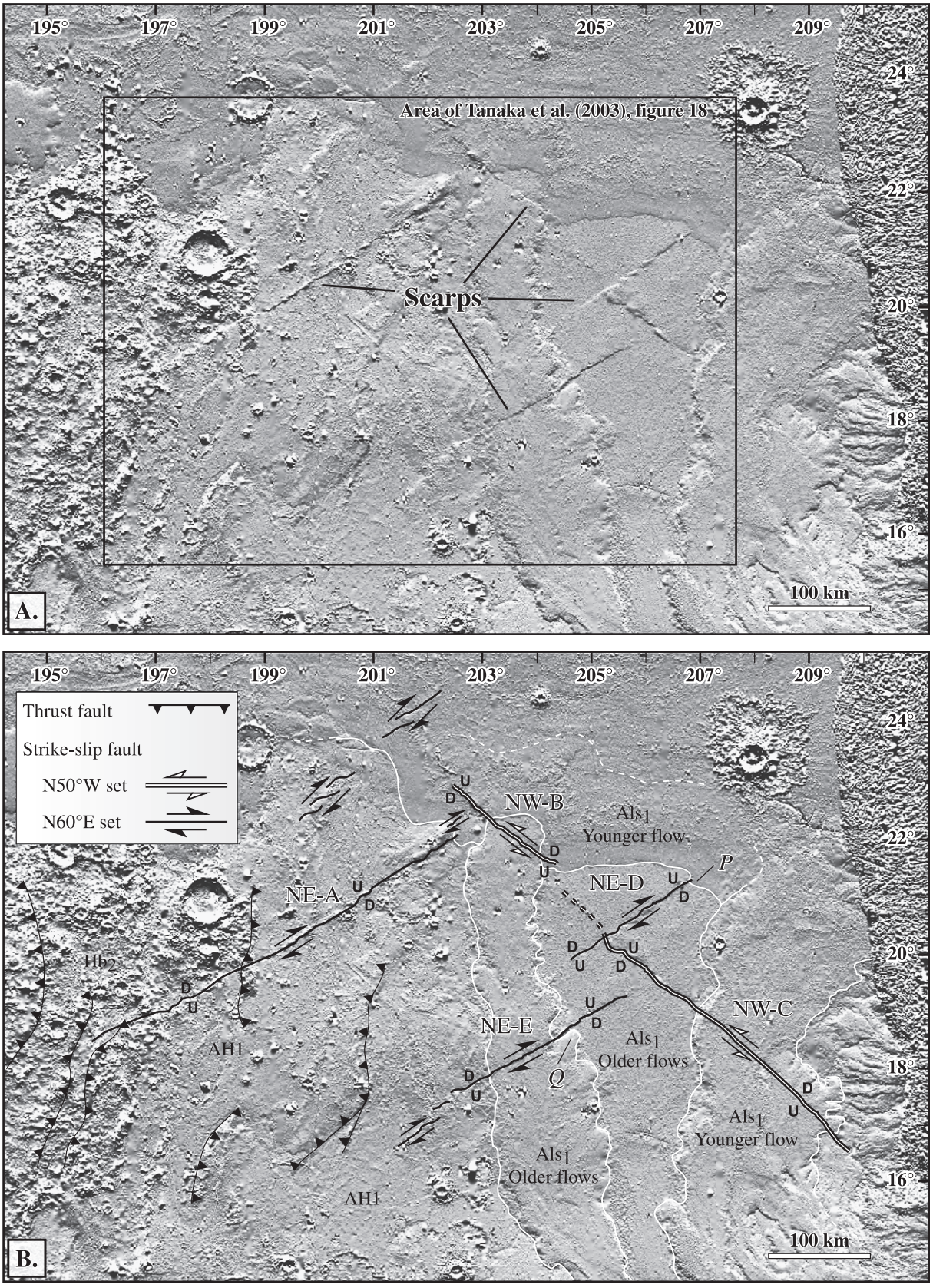

Fig. 2. MOLA-based shaded relief map of the study area. Illumination is from the north, and the image is in a Mercator projection. (A) Minimally annotated map showing sets of linear scarps identified by Tanaka et al. (2003). (B) Interpreted fault structure and provisional fault names based on the results of this study, with stratigraphic divisions from Tanaka et al. (2003). The sense of uplift (U) and down-drop (D) is noted across the scarps. Points *P* and *Q* refer to apparent lava flow interactions with fault-related topography as discussed in the text.

faults of the N60°E set. Further, the sense of asymmetry in the throw along the N50°W set is opposite to asymmetry along the N60°E set. The northern halves of the N50°W faults show a down-to-the-west sense of throw, while the southern halves of these faults show a down-to-the-east sense of throw. Recall that the northern halves of the N60°E faults show a down-to-the-east sense of throw and the southern halves show a down-to-the-west sense of throw. This asymmetric distribution of throw along the N50°W fault set is very subdued in the shaded relief map of Tanaka et al. (2003, fig. 18 therein), potentially due to their lower DEM resolution. Further, much of the length of the longest N50°W fault (fault NW-C), which reveals an asymmetric distribution of throw, lies outside of the area shown by Tanaka et al. (2003).

Analysis of fault NW-B (Fig. 2b) shows apparent scarps within a lava flow of the younger unit of Als_1. That same lava flow interacts with apparent fault-related topography of fault NE-D (Fig. 2b, point *P*); the flow margin embays the down-thrown side of the fault and flows around the up-thrown side. These relations are consistent with fault NE-D of the N60°E set predating the lava flow of the younger unit of Als_1, which is in turn cut by fault NW-B, the N50°W fault set. Similarly, a lava flow of the older unit of Als_1 appears to interact with topography related to fault NE-E (Fig. 2b, point *Q*). Thus, here we see evidence that faults of the N60°E set predate faults of the N50°W set, contrary to the interpretations of Tanaka et al. (2003).

The westernmost portion of the study area covers the Hesperian-aged boundary plains unit 2 (Hb_2) of Tanaka et al. (2003). Multiple north–south-trending curvilinear ridges are apparent in this area. Cross-strike topographic profiles of these ridges show asymmetric slopes, which are characteristic of wrinkle ridges (Okubo and Schultz, 2003, 2004). This system of ridges is also interpreted as wrinkle ridges by Scott and Tanaka (1986), which by their stratigraphic classification is part of the Hesperian ridged plains material, a classic wrinkle ridge terrain. Several of these wrinkle ridges are apparently cross-cut by fault NE-A.

In summary, observations of the DEM shown in Fig. 2 suggest that faults of both the N60°E and N50°W sets have asymmetric distributions of throw, and this sense of asymmetry is reversed between the two sets but common within each orientation. The interactions between lava flows and fault-related topography are consistent with the faults of the N50°W set experiencing slip most recently, or at least synchronous with faults of the N60°E set. Although differing in detail from the results of Tanaka et al. (2003), these findings remain consistent with a timing of deformation within the Middle Amazonian.

3. Interpretation

In line with Tanaka et al. (2003), we interpret the N60°E scarp set to be strike-slip faults. Further, we interpret the N50°W set to be strike-slip faults as well, contrary to their identification as wrinkle ridges by Tanaka et al. (2003). We find that slip along the N50°W set is younger than or synchronous with slip along the N60°E set. Our interpretations are based on the apparent asymmetric distribution of throw along both scarp sets and cross-cutting relations with adjacent lava flows. In this section, we detail the observational and mechanical basis for these interpretations, provide a line of reasoning to exclude an origin by dip-slip faulting, and provide an explanation for our interpreted relative ages of the two scarp sets.

3.1. Origin by strike-slip faulting

Observations of terrestrial topography and coseismic displacements related to strike-slip faulting characteristically show an asymmetric distribution of throw along the fault trace (e.g. Bilham and King, 1989; Eberhart-Phillips et al., 2003). Three-dimensional numerical models of the elastic crustal displacements surrounding a strike-slip fault also predict this asymmetric distribution of throw (Chinnery, 1961; ten Brink et al., 1996; Masterlark and Wang, 2002).

An asymmetric distribution of throw arises due to the distribution and relative senses of offset along a fault plane of finite length. Slip along a fault causes compression of the crust within the leading quadrants of that fault and attendant tension within the trailing quadrants (Fig. 3). For a strike-slip fault that has a sub-horizontal slip direction, these resulting stresses cause topographic uplift in the (compressive) leading quadrants of the fault and subsidence in the (tensile) trailing quadrants. The magnitude of this uplift and subsidence is proportional to maximum strike-slip displacement along the fault (ten Brink et al., 1996). Thus, in addition to the primary sub-horizontal

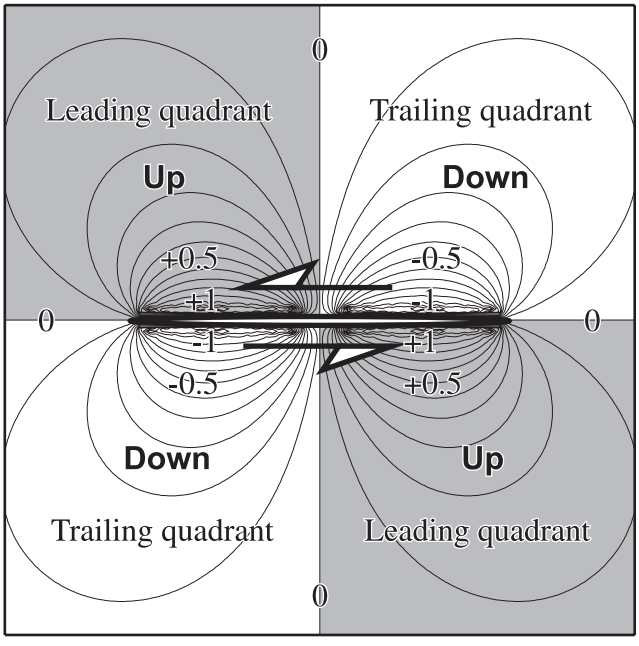

Fig. 3. Illustration of the leading and trailing quadrants of a fault as defined by the sense of displacement along that fault. Also shown are generalized unit contours of strike-slip fault induced topography. Contours show the vertical surface displacement normalized by maximum (positive) uplift. Subsidence is predicted in the trailing quadrants of the fault and uplift is predicted in leading quadrants. Vertical displacements are greatest along the trace of the strike-slip fault and lead to an apparent asymmetric distribution of throw along the fault.

component of along-strike displacement, strike-slip faults also show relative vertical displacements (throw) that are asymmetric along the fault trace.

Just as a consistent along-strike sense of throw can be used to classify thrust or normal faults, an asymmetric along-strike sense of throw can be used to identify strike-slip offsets and the attendant sense of displacement (left- or right-lateral). Since uplift is predicted in the leading quadrants of strike-slip faults and subsidence is predicted in the trailing quadrants, the sense of displacement can be determined from the relative locations of fault-related push-ups and basins, and the corresponding sense of throw, along the trace of the scarp (Fig. 3). Using this principle as a guide, the topography along and adjacent to both faults of the N50°W set corresponds to a consistently left-lateral sense of displacement. Along the faults of the N60°E set, scarp topography consistently corresponds to a right-lateral sense of displacement.

An alternative origin by primarily dip-slip displacement (e.g. thrust or normal faulting) along the N60°E and N50°W scarps can be argued against based on the relative magnitudes of throw versus scarp length. For dip-slip faults, the ratio of the maximum down-dip displacement versus fault length (D_{max}/L) is a common measure of critical fault strain (Cowie and Scholz, 1992a,b). This D_{max}/L ratio is a function of the strength and deformability of the crust (Cowie and Scholz, 1992a; Schultz and Fossen, 2002), as well as fault interaction effects (Cartwright et al., 1995; Schultz and Fossen, 2002) and planetary gravity (Schultz et al., in press). Typical D_{max}/L ratios for faults on Earth are within a narrow range of 1×10^{-1}–1×10^{-2} for various tectonic settings, rock types and sense of displacement (e.g. Cowie and Scholz, 1992a; Schultz and Fossen, 2002). Typical D_{max}/L ratios for thrust and normal faults on Mars range from 1×10^{-2} to 1×10^{-3} (Schultz, 1997; Watters et al., 2000; Wilkins et al., 2002; Schultz et al., in press). Measurements of maximum throw normalized by scarp length (T_{max}/L; equivalent to D_{max}/L for dip-slip faults) from the N60°E and N50°W scarp sets are several orders of magnitude too small to be consistent with an origin by primarily dip-slip faulting.

In order to measure the magnitude and sense of throw across the N60°E and N50°W scarp sets, the MOLA PEDR data that were previously used to create the DEM shown in Fig. 2 are processed using a nearest-neighbor gridding routine to create a discontinuous surface DEM. Individual pixels in this DEM contain values of mean MOLA elevation only, with no interpolated elevations (search radius of the near-neighbor gridding algorithm is equal to pixel width (cf. Okubo et al., 2004)). The DEM is gridded to a resolution of 200 pixels/degree (ca. 279 m/pixel), the same resolution as the continuous surface DEM of Fig. 2. Since the resolution of the DEM approaches the cross-strike length scale of the fault scarps, the discontinuous surface DEM provides more meaningful magnitudes of scarp throw than the continuous surface DEM, which contains numerous pixels of interpolated values that may significantly bias the magnitude of apparent throw.

Topographic profiles are obtained from the discontinuous surface DEM using the program 'gridview' (Roark et al., 2004). The topographic profiles are carefully constructed across the strike of each fault scarp entirely within pixels that contain mean elevation data. Null value pixels (pixels that do not contain averaged MOLA data) are not used. Therefore these measurements do not contain interpolated elevation values. Multiple profiles are constructed across each scarp in order to characterize the distribution of throw and to provide a measurement of apparent scarp length. The ungridded MOLA PEDR track line data are not used here because the data tracks are oriented oblique to the scarp strike and could bias measurements of apparent throw.

The distribution of throw along each fault scarp is shown in Fig. 4. Here magnitudes of throw are normalized by scarp length (T/L) along the y-axis and are plotted against normalized scarp length along the x-axis. The asymmetric distribution of throw along both the N60°E and N50°W scarp sets is clearly shown, as is the consistent sense of asymmetry for individual scarps within each orientation. Further, the relative magnitude of throw scales consistently with scarp length for all faults. The average T_{max}/L ratio for the N60°E and N50°W sets is ca. 3×10^{-5}. Comparison with the equivalent D_{max}/L ratios for Martian dip-slip faults of 1×10^{-2}–1×10^{-3} shows that the observed T_{max}/L ratios for the N60°E and N50°W scarp sets are 2–3 orders of magnitude too small to be consistent with an origin by purely dip-slip faulting.

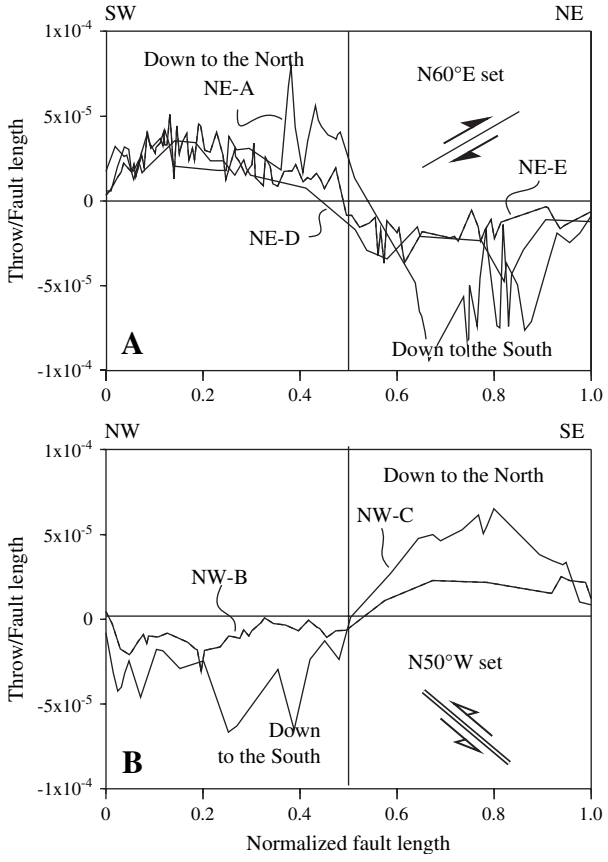

Fig. 4. Distribution of throw along the (A) N60°E scarp set and (B) N50°W set. Asymmetric distributions of throw are recorded along both scarp sets. The ratio of maximum throw to fault length is found to be subequal for all faults regardless of the magnitude of fault length. Down to the north throw is positive.

The distribution of normalized throw shown in Fig. 4 shows high frequency variations in throw superimposed on the longer-wavelength asymmetric distribution. These variations in throw are likely due in part to the sampling frequency of the MOLA instrument. Additionally, these variations can be in part attributed to variations in strike-slip displacement due to interactions between individual hard- or soft-linked fault segments or slip patches, which as a whole constitute the composite strike-slip fault surface. Variability in fault displacement is commonly observed on Earth and is attributed to mechanical interactions between the displacements and stresses induced by slip along adjacent fault segments (Peacock and Sanderson, 1994; Willemse et al., 1996; Willemse, 1997).

An alternative hypothesis for the observed asymmetric distribution of throw along the N60°E and N50°W scarp sets is that these scarps actually represent two dip-slip faults of comparable length and strike, but with opposite senses of vergence, that have met tip to tip at the center of a composite scarp (Fig. 5). The observed T_{max}/L ratios and distributions of throw (Fig. 4), however, argue against this interpretation. Assuming that each segment is composed of two faults of subequal length, the T_{max}/L ratio for each component fault would have the same magnitude of T_{max} but half the value of scarp length. Such modified T_{max}/L ratios would range from 2×10^{-4} to 5×10^{-5} for each putative dip-slip fault within both scarp sets. This T_{max}/L ratio, however, is still ca. 1–2 orders of magnitude too small to be consistent with dip-slip faulting; the putative dip-slip faults do not have realistic magnitudes of throw. Further, the locations of T_{max} on each scarp are evenly distributed relative to the fault tips. If each of these scarps were a composite of two abutting faults, interaction effects would shift the location of the maximum fault displacement toward the intersecting and overlapping fault tips (e.g. Willemse et al., 1996). Clearly this shift in maximum displacement is not observed. Thus this alternative hypothesis of dip-slip faulting is not supported by observations.

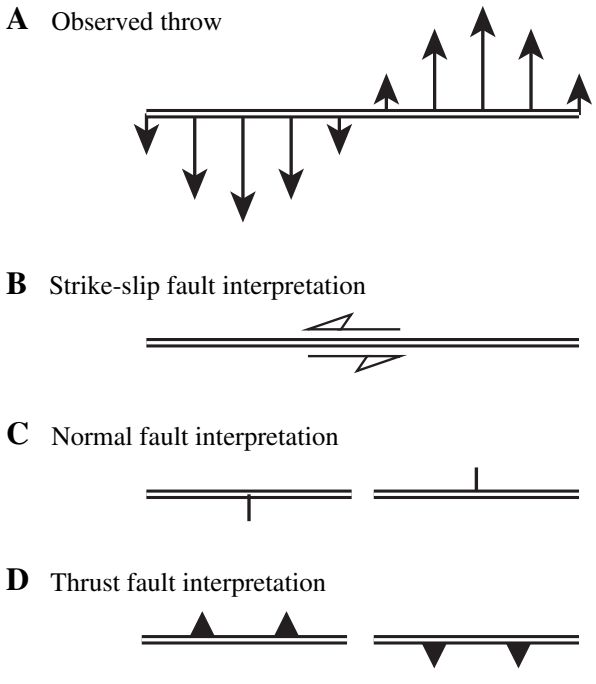

Fig. 5. (A) Generalized asymmetric distribution of throw as observed in the study area. Arrows point toward the down-thrown side of the scarp (double-solid line), and arrow length increases with the magnitude of throw. The favored interpretation of (A) is an origin by (B) strike-slip faulting (compare with Fig. 3). Alternate interpretations of (C) normal and (D) thrust faulting as discussed in the text.

In summary, MOLA-based observations of the N60°E and N50°W scarp sets show that both sets have asymmetric distributions of throw along strike. This pattern of along-strike throw is consistent with patterns that are observed and predicted for strike-slip faults. Further, the magnitudes of maximum throw relative to scarp length are inconsistent with an origin by dip-slip faulting, and the locations and magnitudes of maximum throw along each scarp are inconsistent with an interpretation of two interacting dip-slip faults. Therefore based on these observations and interpretations, both of the N60°E and N50°W scarp sets are interpreted to be the result of strike-slip faulting.

3.2. Relative fault timing and stress state

In order to determine the state of stress at the time of strike-slip faulting, the mechanical relationship between the formation of the N60°E and N50°W scarp sets must be established. Specifically, the possibility that these two sets are conjugate (implying a common causative stress state) must be tested. In this section, we show that the angular relations between the N60°E and N50°W fault sets are consistent with an origin by conjugate faulting. Since the conjugate origin cannot be definitively proven with the available cross-cutting relations, we provide an alternative, non-conjugate, interpretation for the origin of these fault sets as well.

3.2.1. Origin by conjugate faulting?

A population of conjugate faults can be defined by synchronous slip along faults of two distinct orientations that have a friction-dependent angle of separation. As previously stated, cross-cutting relations suggest that fault NW-C of the N50°W scarp set experienced slip most recently and that this activity followed displacement along fault NE-D of the N60°E set. The lack of additional cross-cutting relations, however, means that a conjugate in origin for these fault sets cannot be ruled out. The available cross-cutting relations alone are insufficient to support or dispute a conjugate origin. Alternatively, the magnitude of the acute angular separation between the two fault sets does provide a test of the conjugate origin.

The magnitude of the acute angle of separation between two conjugate fault sets is a function of the friction angle of the intact rock or rock mass. Calculation of the acute angle of separation is cast in terms of the angle, θ, between the maximum compressive stress, σ_1, direction and either conjugate

fault plane; the σ_1 direction bisects the acute angle of separation, which is thus 2θ. The angle θ is given by

$$\theta = 45 - \frac{\phi}{2} \quad (1)$$

(Jaeger and Cook, 1979). At the scale of the N60°E and N50°W fault sets, a rock mass based angle of friction is most appropriate since faulting involves not only slip within intact blocks of rock, but also slip along preexisting faults, fractures and other discontinuities (cf. Hoek, 1983; Schultz, 1996). Typical friction angles for near-surface basaltic rock masses on Mars range from 14 to 25° (Schultz, 2002). These friction angles correspond to an acute angular separation of 65–76° for conjugate faults. The acute angular separation between the N60°E and N50°W fault sets is approximately 70°, and therefore these strike-slip faults may plausibly be conjugate in origin. The opposing senses of slip, right lateral on the N60°E set and left lateral on the N50°W set, is also consistent with a conjugate interpretation for these faults.

Although the sense of slip and angular separation between the N60°E and N50°W fault sets support a conjugate interpretation, this angle is non-unique and by itself is not proof of a conjugate origin. A conjugate origin is desirable because it implies that both fault sets formed under a common far-field stress state, and complex variations in causative stress state are not required. An alternative scenario consistent with an origin under a common far-field stress state is that the growth of one set of faults reactivated slip along the second set. In this scenario, slip along the N60°E faults may have triggered slip along preexisting, possibly buried, fractures in the N50°W orientation.

3.2.2. Insight from Coulomb stress change

Observations and numerical models of coseismic displacements on Earth show that initial slip along a fault induces local stress changes that can either trigger or hinder subsequent slip events along adjacent faults (e.g. King et al., 1994; Lin and Stein, 2004). This distribution of enhanced and reduced tendencies for future slip events is commonly quantified by calculating the change in the Coulomb failure stress, ΔCFS, resolved along potential slip planes following the initial slip event. Coulomb failure stress is the difference between the resolved shear stress and the frictional strength of the fault plane

$$\mathrm{CFS} = \tau - \mu\left(\sigma_\mathrm{n} - p\right) \quad (2)$$

where τ is the resolved shear stress, μ is the coefficient of friction, σ_n is the resolved normal stress, and p is pore fluid pressure within the fault (King et al., 1994). Since τ and σ_n are resolved from effective principal stresses, the magnitude of CFS for any point along a fault plane can change in response to local stresses induced by slip along adjacent faults.

Thus the potential for an initial slip event along a 'source' fault to trigger or hinder future slip along an adjacent 'receiver' fault is recognized as an important process on Earth (e.g. King et al., 1994; Masterlark and Wang, 2002; Lin and Stein, 2004). On Mars, numerical model predictions of ΔCFS have been used to demonstrate potential stress triggering relationships between normal faults in the Valles Marineris region (Wilkins and Schultz, 2003). In our study area, a slip triggering relationship between the N60°E and N50°W fault sets presents a potential alternative to an origin by conjugate faulting. Potentially, strike-slip displacements along faults of the N60°E set triggered slip along faults of the N50°W set, under a common remote stress state.

In order to test a slip triggering relationship between the N60°E and N50°W fault sets, we use the 3-D boundary element program COULOMB (Toda et al., 1998), which was developed in part to study stress triggering of terrestrial strike-slip faults. COULOMB calculates ΔCFS along a prescribed observation plane, also known as the receiver fault. ΔCFS arises due to local stresses that are induced within the crust due to slip along a 'source' fault. COULOMB calculates the ΔCFS along a receiver fault due to prescribed slip along source faults, as well as the corresponding optimal slip directions along that receiver fault.

The potential for slip along faults of the N60°E set to trigger slip along faults of the N50°W set is evaluated by modeling faults NE-D and NE-E as source faults and the plane of fault NW-C as the receiver. Source fault NE-D is also progressively lengthened into the present-day geometry to see the effects that the growth of this fault may have had on receiver fault NW-C. The length of NE-E is kept constant to simplify the analysis; more intricate analyses of fault interactions within the study area will be reported in a future paper. Initially source fault NE-D is prescribed to be 17.15 km long, with its northern tip 22.11 km distant from the receiver plane (Fig. 7a). Subsequently, fault NE-D is lengthened to 61.37 km and its northern tip intersects the receiver plane (Fig. 7b). Finally, the current NE-D fault length of 146.95 km is modeled (Fig. 7c). Both faults NE-D and NE-E extend to 15 km depth, and both have a $D_{\max}/L$ ratio of 6×10^{-3}. $D_{\max}$ (maximum strike-slip displacement) is located at the center of each source fault, along with an elliptical slip distribution within the central region of the fault and a linear tapered displacement within $0.1L$ of the fault tips.

The model stress state is based on an assumed rock mass friction angle, ϕ, of 20° (after Schultz, 2002). Therefore by Eq. (1), σ_1 is oriented 35° from the plane of source fault NE-D. In order to drive the required sense of slip along both faults NE-D and NE-E (right-lateral) and NW-C (left-lateral), σ_1 is prescribed to act along the N95°E direction, bisecting the two fault orientations. Further, the intermediate principal stress (σ_2) is vertical, and the least principal stress (σ_3) is prescribed to act along the N5°E direction, consistent with an Andersonian stress state for strike-slip faulting (Fig. 6) (Anderson, 1951).

The relative magnitudes of the model σ_1 and σ_3 are defined by the Coulomb failure criterion in principal stress form

$$\sigma_1 = \sigma_\mathrm{c} + q\sigma_3 \quad (3)$$

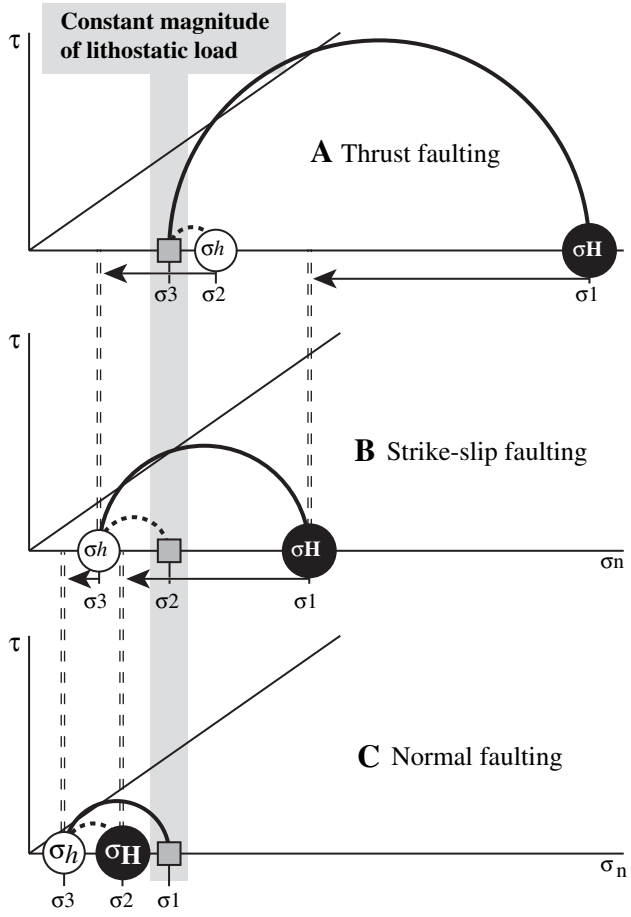

Fig. 6. Andersonian stress states (Anderson, 1951) shown on Mohr circle diagrams. σ_H is the greatest magnitude horizontal compressive stress, and σ_h is the least horizontal compressive stress. The magnitude of the vertical stress (square symbol) is assumed to be equal to a non-trivial lithostatic load that is constant across all stress states. σ_H, σ_h, and the vertical stress are assigned principal stress designations according to their relative magnitudes. Progressive decreases in the magnitudes of the horizontal stresses (arrows) can lead to transitions from (A) a thrust fault stress state, to (B) a strike-slip stress state, to (C) a normal fault stress state.

where

$$\sigma_c = 2C\left(\sqrt{\mu^2+1}+\mu\right) \tag{3a}$$

$$q = \left(\sqrt{\mu^2+1}+\mu\right)^2 \tag{3b}$$

and

$$\mu = \tan\left(\phi\right) \tag{3c}$$

Assuming that the rock mass is sufficiently fractured such that cohesion, C, is negligible (e.g. Hoek and Brown, 1997), the ratio of σ_1 to σ_3 can be approximated by q. With ϕ equal to 20°, σ_1 is thus approximately two times σ_3. If the magnitude of σ_2 is assumed to be equal to a non-trivial lithostatic load then the magnitude of σ_1 is greater than lithostatic load and σ_3 is less than lithostatic load. Thus the model principal stresses can be roughly estimated as $\sigma_1 \approx 15$ MPa/km, $\sigma_2 \approx 10$ MPa/km, and $\sigma_3 \approx 7.5$ MPa/km, assuming a crustal density of 2700 kg/m^3 and gravitational acceleration of 3.71 m/s^2. A rough estimation of the far-field principal stresses is adequate for the purposes of this discussion and a natural range of variations in these magnitudes will not invalidate our general conclusions of stress change. The most important constraints on the causative principal stresses for the purposes of our models are their relative magnitudes ($\sigma_1 > \sigma_2 > \sigma_3$) and orientations being consistent with an Andersonian stress state for strike-slip faulting (Fig. 6).

Fig. 8 shows the results of our numerical models. Areas of positive ΔCFS, where the tendency for frictional slip is enhanced, are shown in grayscale. Areas of negative ΔCFS, where frictional slip is impeded, are shown in black. Specifically, Fig. 8 shows the maximum ΔCFS along the plane of the receiver fault (i.e. fault NW-C). ΔCFS is calculated for the receiver fault orientation, rather than the optimal fault orientation, with no prescribed constraint on the sense of slip. Further, ΔCFS is calculated from the total effective principal stresses, which is the sum of the remote principal stresses plus local stresses induced by slip along the source faults NE-D and NE-E. Vectors in Fig. 8 show the displacement directions of the northeast side of receiver fault NW-C that corresponds with this maximum ΔCFS.

In the initial model configuration, where the southwest tip of source fault NE-D is 22.11 km distant from receiver fault NW-C (Fig. 7a), the tendency for left-lateral slip is enhanced along the receiver between ca. 50 and 82 km to the northwest of the along-strike projection of source fault NE-D (Fig. 8, A–A′). Interestingly, right-lateral slip is enhanced along sections of the plane of the receiver fault. Right-lateral slip is enhanced beyond ca. 82 km to the southwest and between 0 and 60 km to the northwest of the along-strike projection of source fault NE-D. Right-lateral slip is opposite to the left-lateral sense of slip exhibited by the current topography.

Where source fault NE-D intersects receiver fault NW-C (Fig. 7b), a lobe of enhanced dip-slip along the receiver is predicted below 5 km depth and within 20 km of fault NE-D (Fig. 8, B–B′). Slip is impeded at shallower depths and along fault NE-D to the southwest. Strike-slip along the receiver is greatly enhanced to the northeast of the intersection with NE-D. The distribution of enhanced strike-slip is otherwise similar to initial model configuration (Fig. 8, A–A′).

In the present-day fault geometry (Fig. 7c), the tendency for left-lateral slip along the receiver fault is enhanced between fault NE-D and the along-strike projection of fault NE-E (Fig. 8, C–C′). A shallow lobe of enhanced left-lateral strike slip also extends beyond 20 km to the northeast of the intersection with fault NE-D. Strike-slip along the receiver is otherwise impeded beyond 80 km southwest and beyond 20 km northwest of this intersection. The decreased tendency for slip beyond 20 km northwest of NE-D may explain the subtle topography of the receiver fault (NW-C) along this segment.

Results of our ΔCFS models show that left-lateral slip along fault NW-C can be triggered by slip along faults NE-D and NE-E. This slip triggering is strongest in the present-day fault

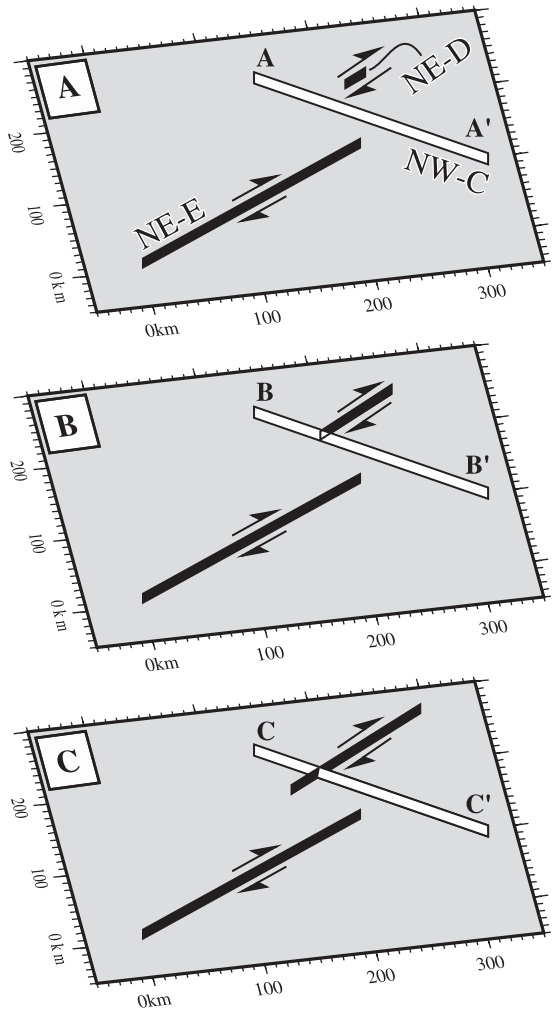

Fig. 7. Three-dimensional perspective view of the modeled source fault NE-E and NE-D (solid black) and modeled receiver fault NW-C (white) geometries, with no vertical exaggeration. The predicted distribution of ΔCFS along the receiver fault for each lettered geometry (A–A′, B–B′, C–C′) corresponds to the identically lettered panels in Fig. 8.

geometry. Thus ΔCFS due to slip along faults of the N60°E set may have nucleated slip along preexisting fractures along the N50°W orientation. A candidate preexisting northwest-trending fracture set may be the regional joint system within the stratigraphically older Medusae Fossae Formation.

The analyses presented in this section show two plausible origins for the faults of the N60°E and N50°W sets slipping under a common stress state. These fault sets may be conjugate in origin, implying synchronous slip along both sets of faults. Alternatively, slip along the faults of the N60°E set may have triggered slip along the faults of the N50°W orientation. In both cases, we have shown how the apparent senses of strike-slip faulting along the N60°E and N50°W sets can plausibly occur under a common stress state, where σ_1 acts in a roughly N95°E orientation, σ_3 acts roughly in a N5°E direction, and σ_2 is vertical. The magnitude of σ_1 is greater than lithostatic load, σ_2 is assumed to be equal to lithostatic load, and σ_3 is less than lithostatic load. Further, the magnitude of σ_1 is approximately twice that of σ_3. The effects of pore fluid pressure on slip triggering (e.g. Masterlark and Wang, 2002) are not explicitly modeled here due to the limitations of COULOMB. Pore fluid effects are expected to enhance the potential for slip along the receiver faults (the N50°W set) by decreasing the frictional strength of these fault planes (e.g. Beeler et al., 2000). Thus the general predictions of our numerical models remain insightful for the purpose of this paper.

4. Discussion

Identification of the N50°W and N60°E scarp sets as contemporaneous strike-slip faults enables a systematic interpretation of the local stress state during the Middle Amazonian, which in turn can provide insight into the local Tharsis-related state of stress at that time. The inferred principal stress directions for the strike-slip faults roughly align with Tharsis-radial and -circumferential stress directions. Thus the relative magnitudes of the principal stresses required for an Andersonian stress state for strike-slip faulting can be used to constrain the relative magnitudes of these Tharsis-related stresses.

During the period of strike-slip faulting in the Middle Amazonian, the inferred direction of the causative σ_3 stress is aligned with the Tharsis-circumferential stress direction, and the direction of σ_1 is consistent with a Tharsis-radial stress (Fig. 9). Therefore the relative magnitude of the Tharsis-radial stress at this time is approximately twice as large as the Tharsis-circumferential stress. Further, the magnitude of the Tharsis-radial stress is greater than lithostatic load, and the magnitude of the Tharsis-circumferential stress is less than lithostatic load. Although the absolute magnitude of lithostatic load is not constrained by this analysis, these relative magnitudes and orientations of the causative principal stresses are bounded by the requirements for an Andersonian state of stress for strike-slip faulting.

Similarly, observations of thrust faults (wrinkle ridges) in the adjacent (pre-Amazonian) boundary plains unit can be used to infer the local state of stress during the Late Hesperian. Given the general north–south trend of these thrust faults, and assuming an Andersonian causative stress state for thrust faulting, the orientation of σ_1 would have been roughly east–west during the stage of active thrust faulting (Fig. 9). Recall that this is the same general σ_1 orientation (Tharsis-radial) for the younger strike-slip faults. Further, σ_2 would need to be oriented roughly north–south (Tharsis-circumferential) and σ_3 would need to be vertical in order to drive slip along these thrust faults. Again assuming that the vertical principal stress is equal to a non-trivial lithostatic load, the magnitudes of σ_2 and σ_1 would have to be greater than lithostatic load at this time. Additionally, the magnitude of σ_1 would be approximately twice that of lithostatic load, assuming a crustal friction angle of ca. 20°.

Therefore, identification of Late Hesperian-aged thrust faults adjacent to Middle Amazonian-aged strike-slip faults provides evidence for a change in the local stress state (Figs. 7 and 9). During the Late Hesperian, the magnitude of the Tharsis-radial stress was greater than the Tharsis-circumferential stress, which was in turn greater than the magnitude of lithostatic load. By the Middle Amazonian, however, the magnitude

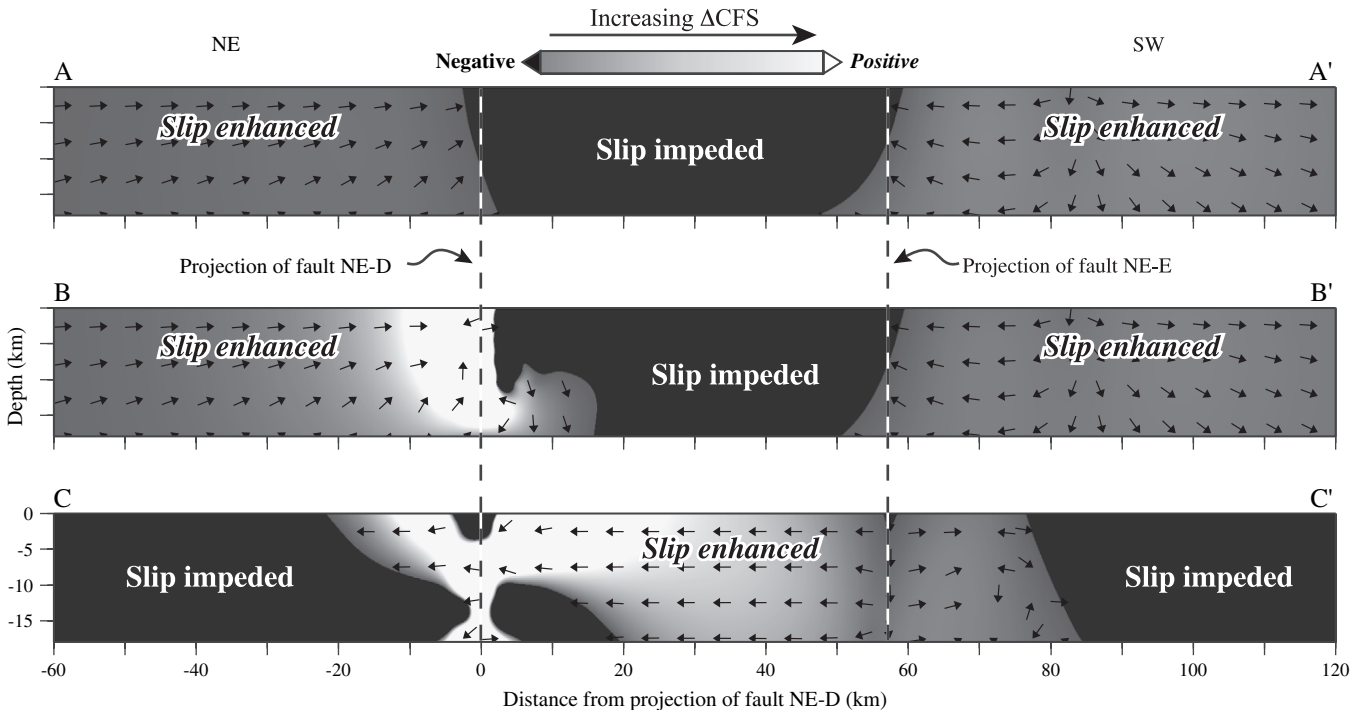

Fig. 8. The predicted distribution of ΔCFS along the plane of the receiver fault for the modeled fault geometries. Each lettered fault plane (A–A′, B–B′, C–C′) corresponds to the identically lettered fault geometries in Fig. 7. Frictional slip along the receiver fault is enhanced toward the white regions and is impeded in the black areas. Arrows indicate optimal slip directions (rake). The tendency for left-lateral triggered slip is greatest in the current fault geometry (C–C′).

of the Tharsis-circumferential stress decreased to less than the magnitude of lithostatic load, while the magnitude of the Tharsis-radial stress remained greater than lithostatic load. Such a change can be readily accomplished by a decrease in the magnitude of both horizontal stresses (Tharsis-radial and -circumferential) between the Late Hesperian and Middle Amazonian (Fig. 6). Continued decrease in the horizontal stress magnitudes would result in lithostatic load being the greatest principal stress (σ_1), a stress state conducive for normal faulting (Fig. 6) (Anderson, 1951).

Such changes in the relative magnitudes of the principal stresses provide a plausible constraint on the timing of wrinkle ridge formation. The end of extensive wrinkle ridge formation, during Late Hesperian, may have been brought about by a decrease in the horizontal crustal stresses such that the magnitude of the Tharsis-circumferential stress was less than the magnitude of lithostatic load, with negligible change in stress orientation. This would lead to a transition from a thrust fault causative stress state (Figs. 6a and 9) to a strike-slip causative stress state (Figs. 6b and 9), impeding further wrinkle ridge formation and promoting strike-slip faulting.

Along a similar path of logic, the beginning of wrinkle ridge time, during the Early Hesperian, may have been brought about by an increase in horizontal crustal stresses, which induced a transition from a stress state conducive to normal faulting (Fig. 6c), to a strike-slip stress state (Fig. 6b), then finally to a thrust faulting-conducive stress state (Fig. 6a). Therefore the beginning and end of wrinkle ridge time may have been simply constrained by systematic changes in the magnitudes of the horizontal principal stresses.

Interpretations of Tharsis-radial graben formation during the Early to Middle Amazonian are admissible under the inferred strike-slip stress state if these grabens formed in response to dike intrusion (Mège and Masson, 1996; Wilson and Head, 2002; Schultz et al., 2004). This is because in the inferred strike-slip stress state, σ_1 is radial to Tharsis and σ_3 is concentric about Tharsis. Since dikes propagate parallel to σ_1 and σ_2 (Anderson, 1951), this stress state is conducive to the propagation of (vertical) Tharsis-radial dikes. Alternatively, graben formation by purely tectonic normal faulting is admissible if the magnitudes of both horizontal principal stresses were less than lithostatic load (Fig. 6c) with negligible change in stress orientation.

The inferred change in stress state can provide an insight into elastic stress models for Tharsis during the Late Hesperian and Middle Amazonian, subsequent to larger-scale Tharsis loading events that may have occurred during the Noachian (e.g. Phillips et al., 2001). Considering the location of the study area relative to the Tharsis high, the thrust fault stress state inferred for the Late Hesperian is most consistent with flexural loading (Banerdt et al., 1992; Banerdt and Golombek, 2000). The change from thrust faulting to strike-slip faulting represents a distinct change in the local stress state that may be attributable to increasing isostatic compensation of the Tharsis volcano–magmatic pile. Late stage isostatic compensation could also help to explain the discrepancy between the predicted and observed gravity in flexure-only models of Tharsis loading (Phillips et al., 2001). The proposed timing for the transition from flexural loading to isostatic compensation may be a fruitful area of future work in understanding the evolution of mantle viscosity as Tharsis developed.

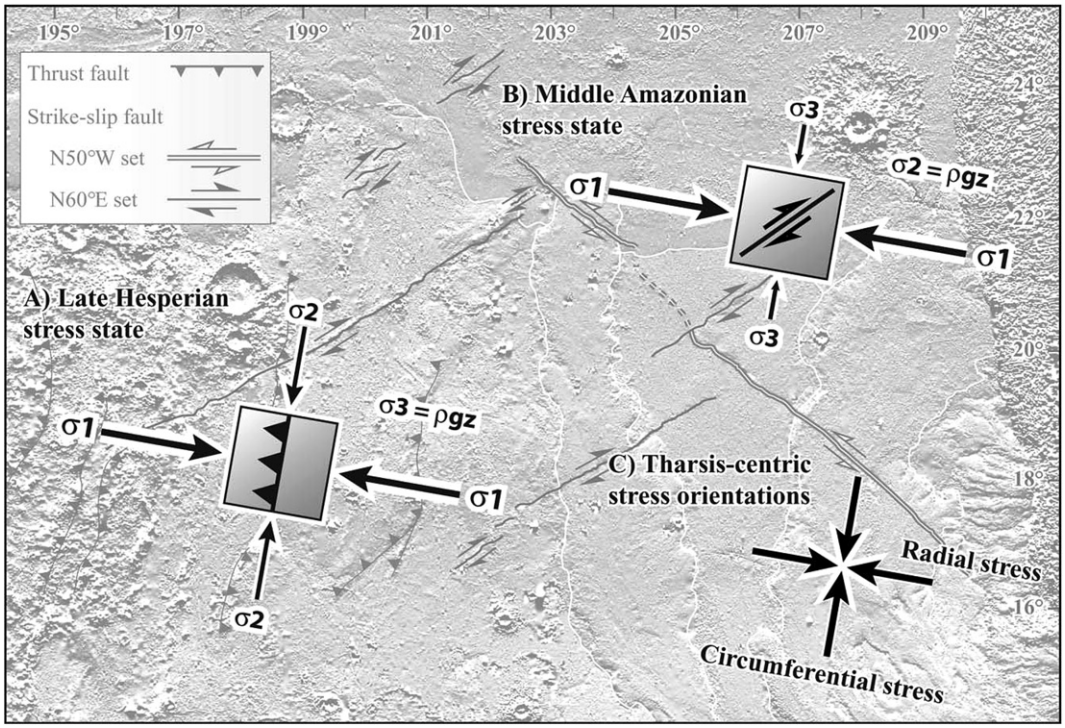

Fig. 9. Inferred stress states during the (A) Late Hesperian thrust faulting period and (B) Middle Amazonian strike-slip faulting period. The vertical stress is assumed to be equal to lithostatic load (see also Fig. 6). The transition from Late Hesperian thrust faulting to Middle Amazonian strike-slip faulting is consistent with a decrease of the horizontal stress acting in the Tharsis-circumferential orientation (C) to a magnitude less than lithostatic load.

5. Conclusions

We identify two sets of Middle Amazonian-aged strike-slip faults in southern Amazonis Planitia. These strike-slip faults are adjacent to a population of Late Hesperian-aged thrust faults (wrinkle ridges). These close spatial and distinct temporal relationships yield insight into the temporal variability of the Tharsis-related stress state. The transition from Late Hesperian thrust faulting to Middle Amazonian strike-slip faulting is attributed to a decrease in the magnitudes of the principal horizontal compressive stresses, with negligible change in stress orientation. This relative change in stress state can be attributed to increasing isostatic compensation between the Late Hesperian and the Middle Amazonian. This change in stress state provides a plausible explanation for the cessation of wide-spread thrust faulting and wrinkle ridge formation by the Early Amazonian. Wide-spread thrust faulting is favored under flexural loading that prevailed during the Late Hesperian. The onset of isostatic compensation during the end of the Hesperian and into the Early Amazonian may have induced a change in the local stress state that favored strike-sip faulting and inhibited further wrinkle ridge development.

Acknowledgements

The authors thank Laurent Montési and Matthew Golombek for thoughtful reviews of this paper. This work is supported by a grant from NASA's Planetary Geology and Geophysics Program.

References

Allemand, P., Thomas, P., 1992. Brittle deformation model for Martian ridges constrained by surface geometry. Comptes Rendus de l'Académie des Sciences-Series IIA 315, 1397–1402.

Anderson, E.M., 1951. The Dynamics of Faulting and Dyke Formation, with Applications to Britain. Oliver & Boyd, Edinburgh.

Anderson, R.C., Dohm, J.M., Golombek, M.P., Haldemann, A.F.C., Franklin, B.J., Tanaka, K.L., Lias, J., Peer, B., 2001. Primary centers and secondary concentrations of tectonic activity through time in the western hemisphere of Mars. Journal of Geophysical Research 106, 20563–20586, doi:10.1029/2000JE001278.

Anguita, F., Farelo, A.-F., López, V., Mas, C., Muñoz-Espadas, M.-J., Márquez, Á., Ruiz, J., 2001. Tharsis dome, Mars: new evidence for Noachian–Hesperian thick-skin and Amazonian thin-skin tectonics. Journal of Geophysical Research 106, 7577–7590, doi:10.1029/2000JE001246.

Artita, K.S., Schultz, R.A., 2005. Significance of deformation band-like strike-slip faults on Mars. 36th Lunar and Planetary Science Conference, Abstract 2225.

Banerdt, W.B., Golombek, M.P., 2000. Tectonics of the Tharsis region of Mars: insights from MGS topography and gravity. 31st Lunar and Planetary Science Conference, Abstract 2038.

Banerdt, W.B., Golombek, M.P., Tanaka, K.L., 1992. Stress and tectonics on Mars. In: Kieffer, H.H., Jakosky, B.M., Snyder, C.W., Matthews, M.S., Gehrels, T. (Eds.), Mars. University of Arizona Press, Tucson, pp. 249–297.

Beeler, N.M., Simpson, R.W., Hickman, S.H., Lockner, D.A., 2000. Pore fluid pressure, apparent friction, and Coulomb failure. Journal of Geophysical Research 105, 25533–25542, doi:10.1029/2000JB900119.

Bilham, R., King, G., 1989. The morphology of strike-slip faults: examples from the San Andreas fault, California. Journal of Geophysical Research 94, 10204–10216, doi:10.1029/89JB00545.

Cartwright, J.A., Trudgill, B.D., Mansfield, C.S., 1995. Fault growth by segment linkage: an explanation for scatter in maximum displacement and

trace length data from the Canyonlands Grabens of SE Utah. Journal of Structural Geology 17, 1319–1326, doi:10.1016/0191-8141(95)00033-A.

Chinnery, M.A., 1961. The deformation of the ground around surface faults. Bulletin of the Seismological Society of America 51, 355–372.

Cowie, P.A., Scholz, C.H., 1992. Physical explanation for the displacement–length relationship of faults using a post-yield fracture mechanics model. Journal of Structural Geology 14, 1133–1148, doi:10.1016/0191-8141(92)90065-5.

Cowie, P.A., Scholz, C.H., 1992. Displacement–length scaling relationship for faults; data synthesis and discussion. Journal of Structural Geology 14, 1149–1156, doi:10.1016/0191-8141(92)90066-6.

Eberhart-Phillips, D., Haeussler, P.J., Freymueller, J.T., Frankel, A.D., Rubin, C.M., Craw, P., et al., 2003. The 2002 Denali Fault earthquake, Alaska; a large magnitude, slip-partitioned event. Science 300, 1113–1118, doi:10.1126/science.1082703.

Forsythe, L.M., Zimbelman, J.R., 1988. Is the Gordii Dorsum escarpment on Mars an exhumed transcurrent fault? Nature 336, 143–146, doi:10.1038/336143a0.

Hoek, E., 1983. Strength of jointed rock masses. Géotechnique 33, 187–223.

Hoek, E., Brown, E.T., 1997. Practical estimates of rock mass strength. International Journal of Rock Mechanics and Mining Sciences 34, 1165–1186, doi:10.1016/S1365-1609(97)80069-X.

Jaeger, J.C., Cook, N.G.W., 1979. Fundamentals of rock mechanics. Chapman and Hall, New York.

King, G.C.P., Stein, R.S., Lin, J., 1994. Static stress changes and the triggering of earthquakes. Bulletin of the Seismological Society of America 84, 935–953.

Lin, J., Stein, R.S., 2004. Stress triggering in thrust and subduction earthquakes, and stress interaction between the southern San Andreas and nearby thrust and strike-slip faults. Journal of Geophysical Research 109, B02303, doi:10.1029/2003JB002607.

Mangold, N., Allemand, P., Thomas, P.G., 1998. Wrinkle ridges of Mars—structural analysis and evidence for shallow deformation controlled by ice-rich décollements. Planetary and Space Science 46, 345–356, doi:10.1016/S0032-0633(97)00195-5.

Mangold, N., Allemand, P., Thomas, P.G., Vidal, G., 2000. Chronology of compressional deformation on Mars: evidence for a single and global origin. Planetary and Space Science 48, 1201–1211, doi:10.1016/S0032-0633(00)00104-5.

Masterlark, T., Wang, H.F., 2002. Transient stress-coupling between the 1992 Landers and 1999 Hector Mine, California, earthquakes. Bulletin of the Seismological Society of America 92, 1470–1486.

Mège, D., Masson, P., 1996. A plume tectonics model for the Tharsis province, Mars. Planetary and Space Science 44, 1499–1546, doi:10.1016/S0032-0633(96)00113-4.

Montési, L.G.J., Zuber, M.T., 2003. Clues to the lithospheric structure of Mars from wrinkle ridge sets and localization instability. Journal of Geophysical Research 108, 5048, doi:10.1029/2002JE001974.

Mueller, K., Golombek, M.P., 2004. Compressional structures on Mars. Annual Reviews of Earth and Planetary Science 32, 435–464, doi:10.1146/annurev.earth.32.101802.120553.

Okubo, C.H., Schultz, R.A., 2003. Thrust fault vergence directions on Mars: a foundation for investigating global-scale Tharsis-driven tectonics. Geophysical Research Letters 30, 2154, doi:10.1029/2003GL018664.

Okubo, C.H., Schultz, R.A., 2004. Mechanical stratigraphy in the western equatorial region of Mars based on thrust fault-related fold topography and implications for near-surface volatile reservoirs. Geological Society of America Bulletin 116, 594–605, doi:10.1130/B25361.1.

Okubo, C.H., Schultz, R.A., Stefanelli, G., 2004. Gridding Mars Orbiter Laser Altimeter data with GMT: effects of pixel size and interpolation methods on DEM integrity. Computers & Geosciences 30, 59–72, doi:10.1016/j.cageo.2003.10.004.

Peacock, D.C.P., Sanderson, D.J., 1994. Geometry and development of relay ramps in normal fault systems. American Association of Petroleum Geologists Bulletin 78, 147–165.

Phillips, R.J., Zuber, M.T., Solomon, S.C., Golombek, M.P., Jakosky, B.M., Banerdt, W.B., Smith, D.E., Williams, R.M.E., Hynek, B.M., Aharonson, O., Hauck, S.A., 2001. Ancient geodynamics and global-scale hydrology on Mars. Science 291, 2587–2591, doi:10.1126/science.1058701.

Roark, J.H., Masuoka, C.M., Frey, H.V., 2004. Gridview: recent improvements in research and education software for exploring Mars topography. 35th Lunar and Planetary Science Conference, Abstract 1833.

Schultz, R.A., 1989. Strike-slip faulting of ridged plains near Valles Marineris, Mars. Nature 341, 424–426, doi:10.1038/341424a0.

Schultz, R.A., 1996. Relative scale and the strength and deformability of rock masses. Journal of Structural Geology 18, 1139–1149, doi:10.1016/0191-8141(96)00045-4.

Schultz, R.A., 1997. Displacement–length scaling for terrestrial and Martian faults: implications for Valles Marineris and shallow planetary grabens. Journal of Geophysical Research 102, 12009–12015, doi:10.1029/97JB00751.

Schultz, R.A., 2000. Localization of bedding slip and backthrusts above blind thrust faults: keys to wrinkle ridge structure. Journal of Geophysical Research 105, 12035–12052, doi:10.1029/1999JE001212.

Schultz, R.A., 2002. Stability of rock slopes in Valles Marineris, Mars. Geophysical Research Letters 29, 1932, doi:10.1029/2002GL015728.

Schultz, R.A., Fossen, H., 2002. Displacement–length scaling in three dimensions; the importance of aspect ratio and application to deformation bands. Journal of Structural Geology 24, 1389–1411, doi:10.1016/S0191-8141(01)00146-8.

Schultz, R.A., Watters, T.R., 2001. Forward mechanical modeling of the Amenthes Rupes thrust fault on Mars. Geophysical Research Letters 28, 4659–4662, doi:10.1029/2001GL013468.

Schultz, R.A., Okubo, C.H., Wilkins, S.J., in press. Displacement–length scaling of faults on the terrestrial planets. Journal of Structural Geology, in press.

Schultz, R.A., Okubo, C.H., Goudy, C.L., Wilkins, S.J., 2004. Igneous dikes on Mars revealed by MOLA topography. Geology 32, 889–892, doi:10.1130/G20548.1.

Scott, D.H., Tanaka, K.L., 1986. Geologic map of the western equatorial region of Mars. U.S. Geological Survey Map I-1802-A, scale 1:15,000,000.

Sharpton, V.L., Head, J.W., 1988. Lunar mare ridges: analysis of ridge-crater intersections and implications for the tectonic origin of mare ridges. Proceedings of the Eighteenth Lunar and Planetary Science Conference, 307–317.

Smith, D.E., Zuber, M.T., Frey, H.V., Garvin, J.B., Head, J.W., Muhleman, D.O., et al., 2001. Mars Orbiter Laser Altimeter: experiment summary after the first year of global mapping of Mars. Journal of Geophysical Research 106, 23689–23722, doi:10.1029/2000JE001364.

Smith, D., Neumann, G., Ford, P., Arvidson, R.E., Guinness, E.A., Slavney, S., 2003. Mars Global Surveyor Laser Altimeter Precision Experiment Data Record, NASA Planetary Data System, MGS-M-MOLA-3-PEDR-L1A-V1.0.

Tanaka, K.L., Skinner, J.A., Hare, T.M., Joyal, T., Wenker, A., 2003. Resurfacing history of the northern plains of Mars based on geologic mapping of Mars Global Surveyor data. Journal of Geophysical Research 108, 8043, doi:10.1029/2002JE001908.

ten Brink, U.S., Katzman, R., Lin, J., 1996. Three-dimensional models of deformation near strike-slip faults. Journal of Geophysical Research 101, 16205–16220, doi:10.1029/96JB00877.

Toda, S., Stein, R.S., Reasenberg, P.A., Dieterich, J.H., Yoshida, A., 1998. Stress transferred by the 1995 M_w=6.9 Kobe, Japan, shock: effect on aftershocks and future earthquake probabilities. Journal of Geophysical Research 103, 24543–24566, doi:10.1029/98JB00765.

Watters, T.R., Robinson, M.S., 1999. Lobate scarps and the Martian crustal dichotomy. Journal of Geophysical Research 104, 18981–18990, doi:10.1029/1998JE001007.

Watters, T.R., Schultz, R.A., Robinson, M.S., 2000. Displacement–length relations of thrust faults associated with lobate scarps on Mercury and Mars: comparison with terrestrial faults. Geophysical Research Letters 27, 3659–3662, doi:10.1029/2000GL011554.

Wilkins, S.J., Schultz, R.A., 2003. Cross faults in extensional settings: stress triggering, displacement localization, and implications for the origin of blunt troughs at Valles Marineris, Mars. Journal of Geophysical Research 108, 5056, doi:10.1029/2002JE001968.

Wilkins, S.J., Schultz, R.A., Anderson, R.C., Dohm, J.M., Dawers, N.C., 2002. Deformation rates from faulting at the Tempe Terra extensional province, Mars. Geophysical Research Letters 29, 1884, doi:10.1029/2002GL015391.

Willemse, E.J.M., 1997. Segmented normal faults; correspondence between three-dimensional mechanical models and field data. Journal of Geophysical Research 102, 675–692, doi:10.1029/96JB01651.

Willemse, E.J.M., Pollard, D.D., Aydin, A., 1996. Three-dimensional analyses of slip distributions on normal fault arrays with consequences for fault scaling. Journal of Structural Geology 18, 295–309, doi:10.1016/S0191-8141(96)80051-4.

Wilson, L., Head, J.W., 2002. Tharsis-radial graben systems as the surface manifestation of plume-related dike intrusion complexes: models and implications. Journal of Geophysical Research 107, doi:10.1029/2001JE001593.